

01 Jun 2019

## Lithospheric Structure and Evolution of Southern Africa: Constraints from Joint Inversion of Rayleigh Wave Dispersion and Receiver Functions

Tuo Wang

Stephen S. Gao

*Missouri University of Science and Technology, sgao@mst.edu*

Yuhang Dai

Qiuyue Yang

*et. al.* For a complete list of authors, see [https://scholarsmine.mst.edu/geosci\\_geo\\_peteng\\_facwork/1609](https://scholarsmine.mst.edu/geosci_geo_peteng_facwork/1609)

Follow this and additional works at: [https://scholarsmine.mst.edu/geosci\\_geo\\_peteng\\_facwork](https://scholarsmine.mst.edu/geosci_geo_peteng_facwork)



Part of the [Geophysics and Seismology Commons](#)

### Recommended Citation

T. Wang et al., "Lithospheric Structure and Evolution of Southern Africa: Constraints from Joint Inversion of Rayleigh Wave Dispersion and Receiver Functions," *Geochemistry, Geophysics, Geosystems*, Blackwell Publishing Ltd, Jun 2019.

The definitive version is available at <https://doi.org/10.1029/2019GC008259>

This Article - Journal is brought to you for free and open access by Scholars' Mine. It has been accepted for inclusion in Geosciences and Geological and Petroleum Engineering Faculty Research & Creative Works by an authorized administrator of Scholars' Mine. This work is protected by U. S. Copyright Law. Unauthorized use including reproduction for redistribution requires the permission of the copyright holder. For more information, please contact [scholarsmine@mst.edu](mailto:scholarsmine@mst.edu).

## RESEARCH ARTICLE

10.1029/2019GC008259

### Key Points:

- A 3-D shear wave velocity model is obtained for southern Africa from joint inversion of Rayleigh wave dispersion and receiver functions
- The Okavango dyke swarm and Bushveld intrusion led to crustal underplating and reduced mantle velocities due to lithospheric refertilization
- Thicker crust, lower elevation, and higher crustal  $V_s$  in the Limpopo belt relative to Kaapvaal craton indicate lower crustal eclogitization

### Supporting Information:

- Supporting Information S1

### Correspondence to:

K. H. Liu,  
liukh@mst.edu

### Citation:




Wang, T., Gao, S. S., Dai, Y., Yang, Q., & Liu, K. H. (2019). Lithospheric structure and evolution of southern Africa: Constraints from joint inversion of rayleigh wave dispersion and receiver functions. *Geochemistry, Geophysics, Geosystems*, 20. <https://doi.org/10.1029/2019GC008259>

Received 8 FEB 2019

Accepted 19 JUN 2019

Accepted article online 27 JUN 2019

## Lithospheric Structure and Evolution of Southern Africa: Constraints From Joint Inversion of Rayleigh Wave Dispersion and Receiver Functions

Tuo Wang<sup>1</sup> , Stephen S. Gao<sup>1</sup> , Yuhang Dai<sup>2</sup>, Qiuyue Yang<sup>1</sup>, and Kelly H. Liu<sup>1</sup> 

<sup>1</sup>Geology and Geophysics Program, Missouri University of Science and Technology, Rolla, MO, USA, <sup>2</sup>Department of Ocean Science and Engineering, Southern University of Science and Technology, Shenzhen, China

**Abstract** We conduct a joint inversion of teleseismic receiver functions and Rayleigh wave phase velocity dispersion from both ambient noise and earthquakes using data from 79 seismic stations in southern Africa, which is home to some of the world's oldest cratons and orogenic belts. The area has experienced two of the largest igneous activities in the world (the Okavango dyke swarm and Bushveld mafic intrusion) and thus is an ideal locale for investigating continental formation and evolution. The resulting 3-D shear wave velocities for the depth range of 0–100 km and crustal thickness measurements show a clear spatial correspondence with known geological features observed on the surface. Higher than normal mantle velocities found beneath the southern part of the Kaapvaal craton are consistent with the basalt removal model for the formation of cratonic lithosphere. In contrast, the Bushveld complex situated within the northern part of the craton is characterized by a thicker crust and higher crustal  $V_p/V_s$  but lower mantle velocities, which are indicative of crustal underplating of mafic materials and lithospheric refertilization by the world's largest layered mafic igneous intrusion. The thickened crust and relatively low elevation observed in the Limpopo belt, which is a late Archean collisional zone between the Kaapvaal and Zimbabwe cratons, can be explained by eclogitization of the basaltic lower crust. The study also finds evidence for the presence of a stalled segment of oceanic lithosphere beneath the southern margin of the Proterozoic Namaqua-Natal mobile belt.

### 1. Introduction

Southern Africa comprises the Archean Zimbabwe and Kaapvaal cratons and several mobile belts formed between 2.7 and 0.3 Ga (Figure 1). Assembled before 3.0 Ga, the crust of the Kaapvaal craton is as old as 3.7 Ga in the eastern-southeastern parts of the craton (Compston & Kroner, 1988; Hamilton et al., 1979; Kroner et al., 1996; Thomas et al., 1993). Separated by a NNE trending strike-slip/thrust belt from the oldest core of the craton, the Neo-Archean (3.0–2.5 Ga) crust is exposed on the western side of the craton. The north central portion of the Kaapvaal craton is occupied by the Bushveld complex, which has an estimated age of intrusion of 2.05 Ga (de Wit et al., 1992) and is the largest known layered mafic intrusion in the world (Buick et al., 2001; Von Gruenewaldt et al., 1985; Walraven & Hattingh, 1993). The Zimbabwe craton consists of Archean rocks that formed between 3.6 and 2.5 Ga (Jelsma & Dirks, 2002; Wilson, 1990). The craton was stabilized after an enigmatic regional-scale melting in the crust at about 2.57 Ga, probably due to a delamination event (Hickman, 1978; Treloar & Blenkinsop, 1995). Formed by the collision between the Zimbabwe craton to the north and the Kaapvaal craton to the south at around 2.7 Ga, the Limpopo orogenic belt lies in an east-west trending band and separates the two cratons. Composed of Proterozoic metamorphosed rocks ranging from ~2.0 to ~1.0 Ga, the Namaqua-Natal mobile belt was amalgamated to the Kaapvaal craton during the Namaqua Orogeny between 1.3 and 1.0 Ga, and the youngest tectonic province of the study area, the Cape Fold Belt (0.3 Ga) located at the southern end of Africa, was formed during the late-Proterozoic/early-Cambrian Saldanian Orogeny and the late-Paleozoic Cape Orogeny (Rozendaal et al., 1999).

A number of seismological investigations have been conducted in southern Africa to characterize the thickness, composition, and tectonic evolution of the crust and uppermost mantle. Nair et al. (2006) use receiver functions (RFs) to estimate crustal thickness ( $H$ ) and  $V_p/V_s$  ( $\kappa$ ) using data from the Southern African Seismic Experiment. A thicker than normal crust is observed in the western Zimbabwe craton, the Limpopo

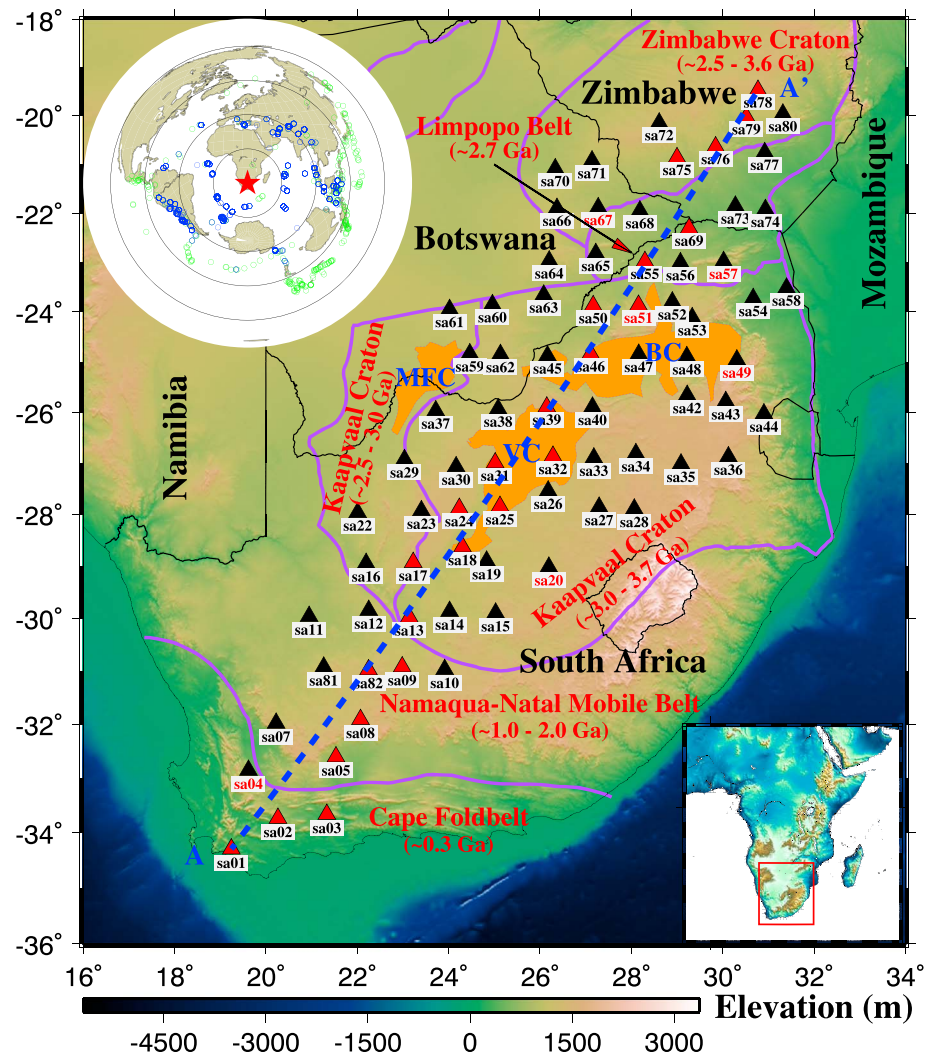


**Figure 1.** An elevation map of the study area showing seismic stations used in the study (triangles) and major tectonic provinces. Stations along profile A-A' (blue dashed line) are marked by the red triangles, and those without reliable receiver function measurements of crustal thickness are marked by red station names. The inset in the upper left corner is an azimuthal equidistant projection map centered at the study area showing the distribution of earthquakes used for receiver function (blue circles) and two-station surface wave dispersion (green circles) analyses. The rectangle area in the inset map in the lower right corner shows the location of the study area. BC, Bushveld complex; VC, Ventersdorp complex; MFC, Molopo Farms complex.

belt, the Bushveld complex, and the Namaqua-Natal mobile belt. The study also reveals a 12-km thickness intruded mafic layer at the bottom of the crust beneath the Bushveld complex. While most other  $H-\kappa$  studies (e.g., Delph & Porter, 2015; Youssof et al., 2013) generally agree with the crustal thickness results of Nair et al. (2006), the resulting  $\kappa$  measurements are more diverse. Youssof et al. (2013) argue a paleocollisional zone rather than a mafic layer intrusion beneath the central part of the Bushveld complex on the basis of the overall felsic composition which is indicated by a low  $V_p/V_s$  of 1.68–1.70, a range that is significantly different from most previous RF studies (e.g., Nair et al., 2006).

Ravenna et al. (2018) perform a surface (Rayleigh and Love) wave phase velocity probabilistic Bayesian inversion to construct shear wave velocity structure beneath the Kaapvaal craton and the Limpopo belt, from the upper crust to the upper mantle. The inverted shear wave velocity curves indicate a thinned lithosphere beneath the central southwestern Kaapvaal craton and a slightly-to-moderately depleted lowermost lithosphere beneath the Limpopo orogenic belt. Yang et al. (2008) obtain shear wave velocities in southern Africa from the surface to 100-km depth using surface wave ambient noise tomography (ANT) for short periods and two-plane-wave method for longer periods. Their results show that velocities in the uppermost crust are

well correlated with the geological units, and high velocities beneath the cratonic regions are mainly due to the existence of more mafic Archean crust. In the uppermost mantle, relatively high velocities are observed under the thinner Archean crust, and low velocities are found beneath the thicker Proterozoic crust (Yang et al., 2008). Using a two-plane-wave tomography technique, Li (2011) and Li and Burke (2006) investigate the approximately same area from surface to 410- and 310-km depths, respectively. Both studies observe that the Bushveld complex is relatively slower than its surrounding areas, suggesting a high iron content from an intracratonic intrusion at 2.05 Ga. Li and Burke (2006) also propose that a low-velocity zone at the depth range of 160 to 260 km across southern Africa is mainly caused by high temperature, which probably supports the high elevation of southern Africa. In contrast, Adams and Nyblade (2011) map shear wave velocities from 50 to 350 km by inverting surface wave phase velocities. Their velocity model is not consistent with the existence of a positive temperature anomaly beneath southern Africa.

Comparing with surface wave tomography, RFs possess the ability to improve the vertical resolution and could better image internal interfaces (Deng et al., 2015; Shen et al., 2013; Shen & Ritzwoller, 2016). However, RFs only provide information near seismic stations and have lower resolution for structures between discontinuities than surface wave tomography (e.g., Ammon et al., 1990). Although southern Africa has been investigated by numerous studies, this study provides a high-resolution 3-D shear wave velocity model from a joint inversion of surface wave dispersion and RFs. To our knowledge, this is the first RF-dispersion joint study to obtain surface wave phase velocity dispersion from both ambient seismic noise (for shorter periods) and teleseismic earthquakes (for longer periods) data for southern Africa. Rayleigh wave phase velocity maps at different periods are obtained by inverting phase velocity dispersion measurements derived from ambient seismic noise at short periods (6–24 s) and teleseismic earthquakes at long periods (28–80 s). Additionally, a nonlinear Bayesian Monte Carlo approach (Shen et al., 2013) is applied to obtain 3-D shear wave velocity model beneath southern Africa.

## 2. Data and Methods

### 2.1. Data

The data used in the study were recorded by 79 Southern African Seismic Experiment seismic stations between April 1997 and December 1999 located in the area of 16–34°E, and 36–18°S (Figure 1). The data set is archived at the Incorporated Research Institutions for Seismology (IRIS) Data Management Center (DMC) and is publicly accessible. For the ANT study, we requested continuous broadband vertical-component waveforms, each with a length of 86,400 s (1 day), from the Incorporated Research Institutions for Seismology DMC. The seismograms were resampled to five samples per second, and Rayleigh wave phase velocity dispersion measurements from 6 to 30 s with an interval of 2 s were then calculated from the empirical Green's function (EGF) analysis (Yao et al., 2006, 2008, 2010). For the two-station earthquake Rayleigh wave phase velocity dispersion measurements (Yao et al., 2005), broadband seismic data with a sampling frequency of 1 Hz were requested from a total of 384  $M_b \geq 5.7$  earthquakes in the epicentral distance range of 10–130°. The period range is from 20 to 80 s with an interval of 4 s.

To compute RFs, data from teleseismic events in the epicentral distance range of 30° to 100° were requested from the DMC. The cutoff magnitude ( $M_c$ ) used for selecting earthquakes is calculated by  $M_c = 5.2 + (\Delta - 30.0)/(180.0 - 30.0) - D/700.0$ , where  $\Delta$  and  $D$  are the epicentral distance in degree and focal depth in kilometer, respectively (Liu & Gao, 2010). A total of 5,653 three-component seismograms from 166 teleseismic events that satisfy the above epicentral distance range and  $M_c$  criterion were chosen for the period of 10 April 1997 to 31 December 1999. The seismograms were windowed 20 s before and 30 s after the first theoretical P-wave arrival based on the IASP91 Earth model (Kennett & Engdahl, 1991).

### 2.2. Methods

#### 2.2.1. Rayleigh Wave Data Processing for ANT

The procedure of data processing used here is generally the same as that in Wang et al. (2019) and is briefly described below. The procedure includes the following steps: (1) single-station preprocessing, (2) cross correlations and temporal stacking, (3) phase velocity dispersion measurements, and (4) inversion for phase velocities. Details about the steps can be found in previous studies (e.g., Bensen et al., 2007; Sabra et al., 2005; Shapiro et al., 2005; Shapiro & Campillo, 2004; Weaver, 2005; Weaver & Lobkis, 2004).

In the single-station preprocessing step, the mean, linear trend, and the instrumental response are first removed, and a second-order Butterworth filter in the frequency range of 0.025–0.5 Hz is utilized, followed

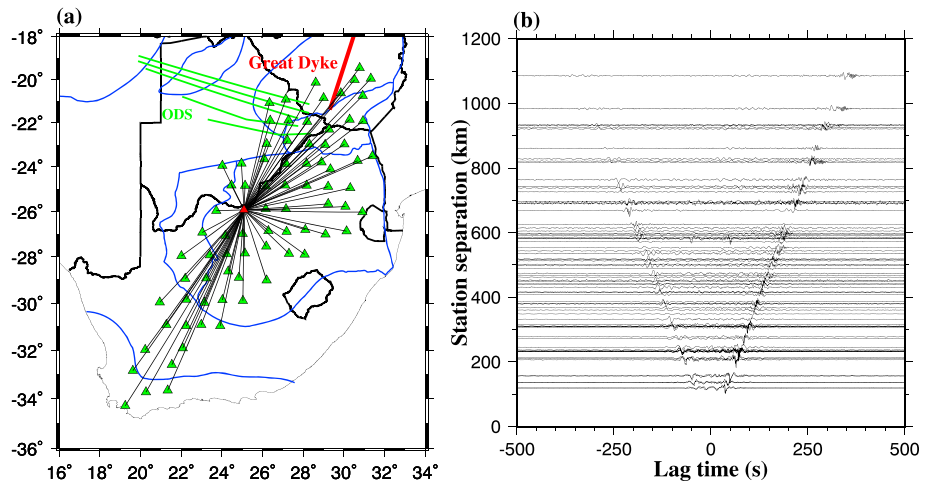


**Figure 2.** (a) Raypaths between Station SA38 (red triangle) and all the rest stations (green triangles). The thick red line in Zimbabwe represents the Great Dyke, and the green lines are the main branches of the Okavango Dyke Swarm (ODS; Le Gall et al., 2002; Uken & Watkeys, 1997). (b) 2- to 40-s band-pass-filtered cross-correlation functions between Station SA38 and the other stations.

by temporal normalization to reduce the interference from earthquakes, instrumental irregularities, and nonstationary noise. Spectral whitening is then applied to produce broadband ambient noise signals.

The next step is to compute cross correlations and perform temporal stacking. The total number of possible daily cross-correlation series is 3081 ( $N = n(n-1)/2$ , where  $n$  is the number of stations). Because not all the 79 stations were operating in a common period, a total of 2,245 possible interstation cross-correlation series were produced. All the daily cross-correlation series for each station pairs are then stacked, and the causal and acausal signals are symmetrically averaged to enhance the signal-to-noise ratio (SNR). A negative time derivative of the stacked cross-correlation series is taken to estimate Rayleigh wave EGFs from the stacked cross-correlation series. Figure 2 shows the raypaths and cross-correlation series between Station SA38 and all the other stations.

Subsequently, phase velocity dispersion curves are estimated from the EGFs based on a modified far-field approximation and an image transformation analysis (Yao et al., 2005, 2006, Yao et al., 2010). Three criteria are imposed to reject unreliable dispersion measurements: (1) the distance between two stations should be at least 3 times of the longest wavelength, (2) the SNR for each of the stacked cross-correlation series should be equal or larger than 5.0, and (3) the phase velocity dispersion curves should be similar to the global model of Shapiro and Ritzwoller (2002).

The final step involves inverting for Rayleigh wave phase velocities using the phase velocity dispersion measurements obtained from the previous step (Tarantola & Nercessian, 1984; Tarantola & Valette, 1982). The phase velocities are for periods between 6 and 30 s with an interval of 2 s, and the horizontal grid dimension is  $0.4^\circ \times 0.4^\circ$  with a sampling step of  $0.1^\circ$ .

### 2.2.2. Rayleigh Wave Data Processing for Earthquake Tomography

The two-station method is utilized to determine fundamental mode Rayleigh wave phase velocities in the period range of 20–80 s (Yao et al., 2005). Based on an image analysis technique (Yao et al., 2004), a MATLAB GUI software is applied to implement the determination of the phase velocity dispersion curves (Yao et al., 2005). The two-station analysis is under the assumption that surface wave propagation is along a great-circle path between the earthquake and station. First, the instrumental responses of station records with clear Rayleigh wave trains are removed. Subsequently, the multiple filter technique (Dziewonski et al., 1969) is applied to determine group arrival times of Rayleigh wave fundamental mode, and to obtain the cross-correlation amplitude image for each of the station pairs. Third, a three-spline interpolation is applied to transform the cross-correlation amplitude image into a phase velocity image for directly judging the quality of phase velocity dispersion curves (Yao et al., 2006). The selected phase velocity dispersion measurements are inverted using the same technique as that applied in the EGF analysis. Phase velocity maps are constructed for periods between 20 and 80 s with an interval of 4 s. The grid dimension and sampling

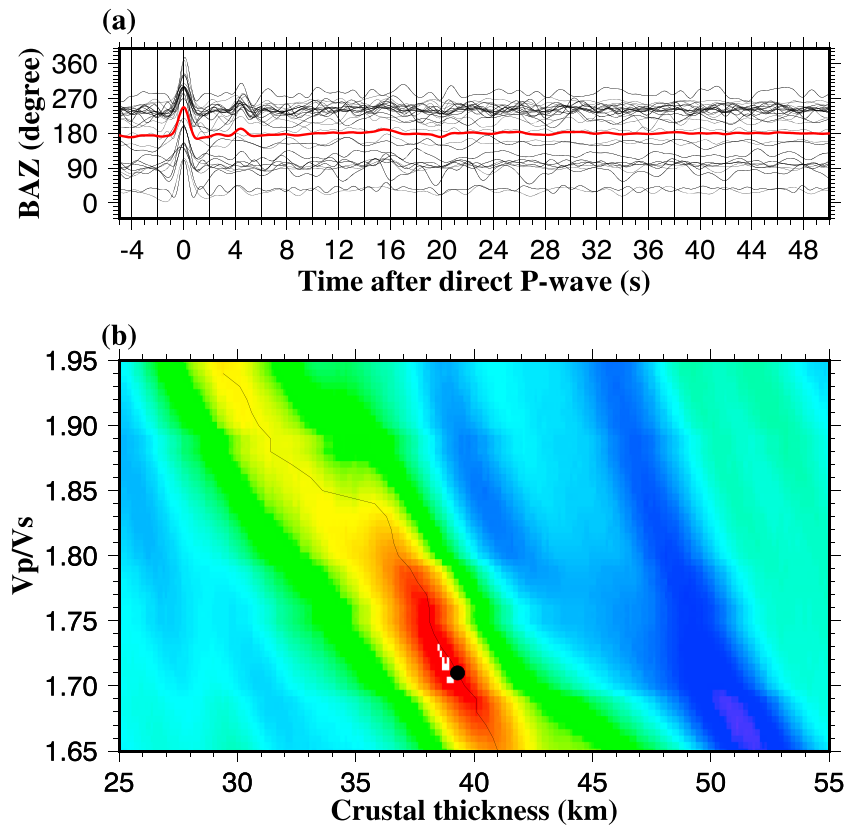


**Figure 3.**  $H - \kappa$  stacking of receiver functions (RFs) from Station SA38. (a) RFs plotted against the back azimuth (BAZ). The red trace is the result of simple time domain summation of the individual traces. (b)  $H - \kappa$  stacking using the RFs in (a).

step are the same as those for the ANT analysis. The study area was divided into  $0.2^\circ \times 0.2^\circ$  grids, and those with at least one raypath were retained.

### 2.2.3. RF Data Processing

A four-pole, two-pass band-pass Bessel filter with a frequency range of 0.06–1.2 Hz is applied to the original seismograms to enhance the signals, and to reject events with SNR of less than 4.0. The SNR is calculated using  $\text{SNR} = \max |A_s| / |\bar{A}_n|$ , where  $\max |A_s|$  represents the maximum absolute amplitude on the vertical seismograms in the time window of 8 s before and 17 s after the predicted IASP91 arrival time for the first  $P$  wave, and  $|\bar{A}_n|$  represents the mean absolute amplitude in the time window of 10–20 s before the predicted  $P$  wave arrival time (Gao & Liu, 2014). We next apply a frequency domain water-level deconvolution procedure (Ammon et al., 1990) to convert the filtered seismograms into radial RFs.

The  $H - \kappa$  RF stacking procedure (Zhu & Kanamori, 2000) is applied to search for the optimal  $H$  and  $\kappa$  pair. The weighting factors used in the study are 0.5, 0.3, and 0.2 for the  $PmS$ ,  $PPmS$ , and  $PSmS$  phases, respectively, which are the same as those in Nair et al. (2006). The mean crustal  $P$  wave velocity ( $V_p$ ) required by  $H - \kappa$  stacking is chosen as 6.5 km/s, which is based on results from a seismic refraction survey (Durrheim & Green, 1992). The use of a uniform crustal  $V_p$  for all the stations may lead to errors in the resulting  $H$  and  $\kappa$  values (Nair et al., 2006). While the error in  $H$  can be reduced by jointly inverting both the RF and surface wave dispersion measurements, that in  $\kappa$  remains unchanged. Consequently, in this study we rely more on the shear wave velocities, which are less affected by the assumed  $V_p$ , than the  $\kappa$  measurements to discuss continental crustal structure and evolution. The bootstrap resampling approach (Efron & Tibshirani, 1986; Press et al., 1992) with 10 iterations is utilized to compute the mean values of  $H$  and  $\kappa$  and to estimate their standard deviations. Figure 3 shows an example of the  $H - \kappa$  diagrams, and more examples can be found in Figures S1–S4 in the supporting information.

### 2.2.4. Joint Inversion of Surface Wave Dispersion and RFs

Surface wave dispersion measurements are sensitive to absolute shear wave velocities and can be used to constrain the vertically averaged velocity profile (Deng et al., 2015). In comparison, RFs can provide reliable

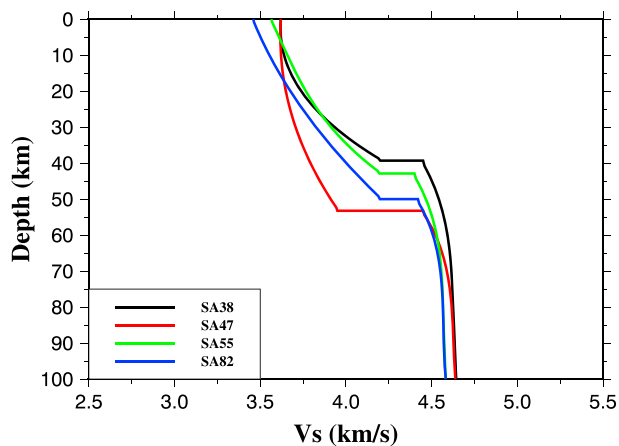


**Figure 4.** Four examples of initial models for the joint inversion. The black line represents initial  $S$  wave model for Station SA38 in the Kaapvaal craton, red line is for Station SA47 in the Bushveld complex, green line is for Station SA55 in the Limpopo belt, and the blue line is for Station SA82 in the Namaqua-Natal mobile belt.

constraints on vertical velocity contrasts, such as the Moho discontinuity and bottom of the sedimentary layer, which are difficult to resolve using surface wave dispersion alone. Consequently, RFs can effectively complement surface wave dispersion (e.g., Bodin et al., 2012; Julia et al., 2000; Ozalaybey et al., 1997), and the results from joint inversion of surface wave dispersion and RFs are more reliable than those obtained on either data set alone (e.g., Julia et al., 2005; Shen et al., 2013). In this study, we apply a nonlinear Bayesian Monte Carlo technique (Shen et al., 2013) to construct a 3-D shear wave velocity structure, from the surface to the depth of 100 km, by jointly inverting Rayleigh wave phase velocity dispersion and RFs. Detailed information about the joint inversion procedure can be found in Shen et al. (2013).

Similar to Shen and Ritzwoller (2016), three prior constraints are employed during the process of the Monte Carlo sampling: (1) shear wave velocity increases from the lower crust to the uppermost mantle through the Moho discontinuity, (2) shear wave velocity monotonically increases with depth through the entire crystalline crust, and (3) shear wave velocity is no more than 4.9 km/s for all depths. Considering the values of  $H$  and  $\kappa$  vary from station to station, we generate one initial model for each of the stations. For stations with reliable RF measurements, Rayleigh

wave phase velocities and RFs (in the time window of 0 to 10 s) are jointly inverted. For stations without reliable RF measurements (SA04, SA20, SA49, SA51, SA57, and SA67), only the surface wave phase velocities are inverted. To estimate uncertainties of the phase velocities for the joint inversion for a given station, the mean and the standard deviation of all measurements at the station are calculated. The initial model includes two layers. The top layer is the crystalline crust, which has a layer thickness  $H$  obtained from the  $H - \kappa$  stacking of RFs, and the bottom layer has a depth range of  $H-100$  km. The shear wave velocities for the crust are obtained using a 4 cubic B-spline interpolation of the velocity model of Yang et al. (2008), and for the subcrustal layer, the interpolation is performed using 5 cubic B-splines. Therefore, for each station, a total of 10 parameters are varied between the iterations, including the crustal thickness, 4 B-spline coefficients for crustal  $V_s$ , and 5 such coefficients for subcrustal  $V_s$ . The allowed magnitude of variation from the values in the initial model is 25% for crustal thickness, and 20% for the coefficients. Scaling relations (Christensen & Mooney, 1995; Karato, 1993) are applied to estimate the densities in the crust and upper mantle. The  $Q$  values in the PREM model (Dziewonski & Anderson, 1981) are utilized to conduct physical dispersion corrections by applying the approach of Kanamori and Anderson (1977). In the crust, the  $\kappa$  values for the initial models are derived from the  $H-\kappa$  stacking of the RFs, while in the upper mantle it is fixed at 1.75. For surface wave dispersion, the Thomson-Haskell method (computed using the code of Herrmann, <https://www.eas.slu.edu/eqc/eqccps.html>) with an earth-flattening transformation was used for the forward modeling, and the forward calculation of RFs is based on the code developed by Shibutani et al. (1996). For each iteration, the root mean square misfit function for both the dispersion and RF measurements are combined after being normalized by the minimum misfit for each data type. Similar to previous studies (Shen et al., 2013, 2016), the number of iterations is 3,000. Figure 4 shows initial models for stations located in different regions.

### 3. Results

#### 3.1. Rayleigh Wave Phase Velocity Tomography

##### 3.1.1. Phase Velocity Maps From ANT

By inverting a total of 515 reliable phase velocity dispersion measurements, 2-D phase velocity maps for the periods of 6 to 30 s are obtained with  $0.4^\circ \times 0.4^\circ$  spatial grids. Figures 5a–5c show phase velocity maps at the periods of 6, 16, and 24 s, respectively. The resulting spatial distribution of phase velocities correspond well with known geological features. At the period of 6 s (Figure 5a), low phase velocity anomalies are observed in the northern and eastern Kaapvaal craton, eastern part of the boundary between the Zimbabwe craton and the Limpopo belt, the Namaqua-Natal mobile belt, and the Cape Fold Belt. The low phase velocity anomalies are mainly attributed to relatively thick sedimentary layers (de Wit et al., 1992; de Wit & Tinker, 2004; Durrheim & Green, 1992; Green & Durrheim, 1990). Relatively high phase velocities are observed in

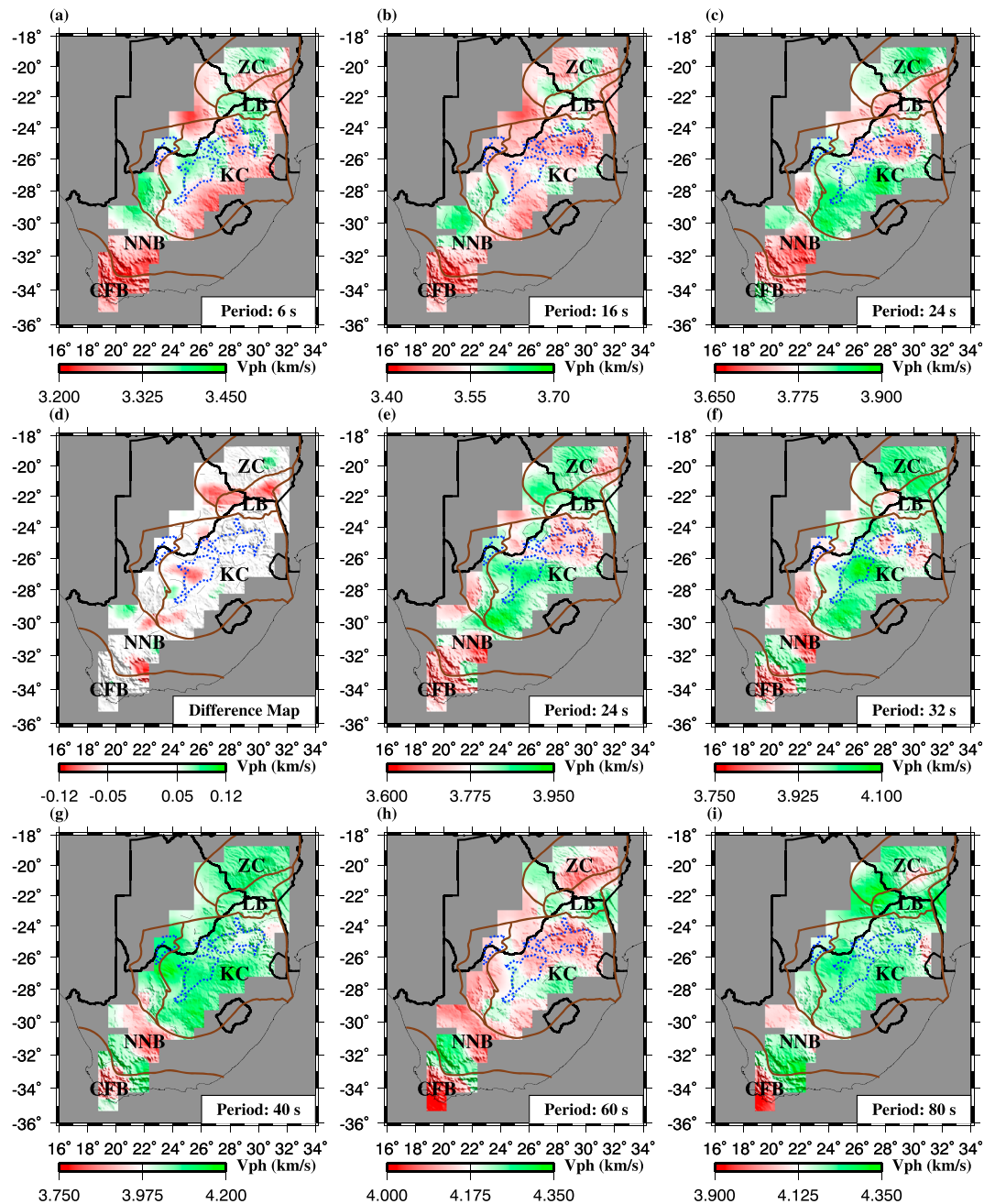


**Figure 5.** Rayleigh wave phase velocity maps from EGF (a–c) and two-station (e–i) analyses. Panel (d) shows the difference between phase velocities from EGF and two-station analyses at the period of 24 s. EGF = empirical Green’s function.

most parts of the Zimbabwe craton and the Limpopo belt, and the central and western Kaapvaal craton, and are most likely due to the existence of a more mafic Archean upper crust (Durrheim & Mooney, 1994). Low phase velocity anomalies observed at the period of 6 s persist at the period of 16 s in most areas (Figure 5b). For the period of 24 s (Figure 5c), the high phase velocities beneath the central Zimbabwe craton expand to the entire cratonic area and become more evident. Most of the southern Kaapvaal craton is characterized by relatively high phase velocities.

### 3.1.2. Phase Velocity Maps From Earthquake Tomography

Phase velocity maps at the period of 24 s from both the EGF and two-station analyses (Figures 5c and 5e, respectively) are plotted for comparison, and Figure 5d shows the differences. The patterns of the



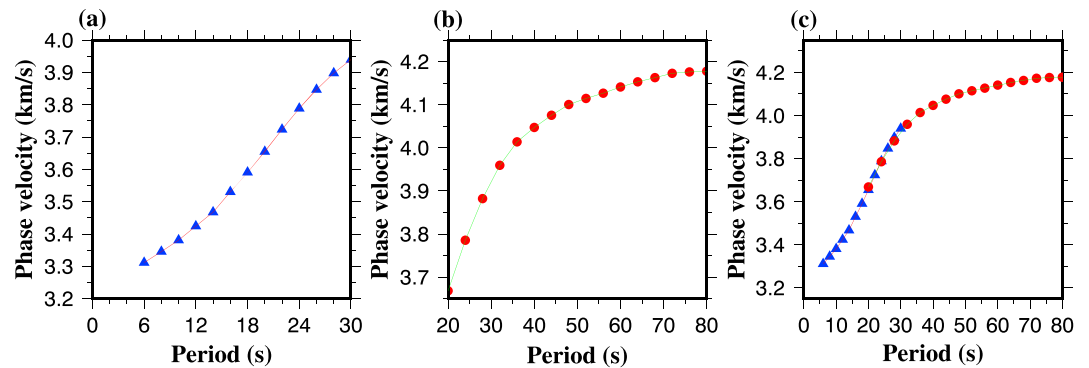


**Figure 6.** Averaged Rayleigh wave phase velocity curves over the entire study area from (a) empirical Green's function analysis, and (b) two-station analysis. (c) Combined result of phase velocity curves for the period range of 6 to 80 s. Note the consistency between the results from the two methods in the overlapping periods (20–30 s).

distribution of the phase velocities are similar with each other, and differences with an absolute amplitude greater than 0.05 km/s are observed only in a few locations (Figure 5d). Considering that the EGF analysis can provide more reliable phase velocity measurements at shorter periods (Yao et al., 2006), we use phase velocity measurements from the EGF analysis for the periods of 6 to 24 s, and those from the two-station analysis for the periods of 28 to 80 s. Figure 6 shows averaged Rayleigh wave phase velocity curves derived from both the EGF and two-station techniques.

At the periods of 32 and 40 s (Figures 5f and 5g), relative to the southern Kaapvaal craton, slow velocities are revealed for the central part of the Bushveld complex, the northern Namaqua-Natal mobile belt, and the Cape Fold Belt. At the period of 60 s (Figure 5h), low velocities appear in the northeastern portion of the Zimbabwe craton and the northern Limpopo belt, the southwestern part of the Kaapvaal craton, and Bushveld and Ventersdrop complex. At the period of 80 s (Figure 5i), the velocities within the southern Kaapvaal craton become comparable with the rest of the study area, except for the Cape Fold Belt which continues to show low velocities.

### 3.2. Resolution Test

We conduct standard synthetic checkerboard test to investigate the resolution of the resulting phase velocities at different periods (Figure 7). For each of the periods, the input velocity model is composed of alternating positive and negative velocity anomalies with a 5% magnitude relative to 4 km/s in  $2.0^\circ \times 2.0^\circ$  blocks (Figure 7a).

The events and stations used to generate the synthetic data are exactly the same as those in the real data, and the same inversion method was applied to obtain the recovery data. Figures 7b–7h show the recovered velocity models for the periods of 6, 16, 24, 32, 40, 60, and 80 s with the same raypath coverage. The pattern of the checkerboard and the magnitude of anomalies can be well reconstructed for all the periods. Even though lateral smearing is more observable at longer periods (e.g., 60 and 80 s), the velocity anomalies are still resolvable in most of the study area. In general, the checkerboard test suggests that the resulting phase velocities are acceptable for all the periods.

### 3.3. Crustal Thickness From RFs

A total of 1,976 high-quality RFs from 164 teleseismic events recorded by 73 out of the 79 seismic stations were used to obtain  $H$  and  $\kappa$  measurements. The resulting  $\kappa$  values (Figure S5) range from 1.68 at Station SA47 located within the Bushveld complex to 1.88 at Station SA03 in the Cape Fold Belt, with an average value of  $1.75 \pm 0.04$ . Most stations within or adjacent to the Bushveld complex exhibit higher  $\kappa$  values than the rest of the study area. The resulting  $H$  values (Figure 8b) range from 28.1 km at Station SA01 in the Cape Fold Belt to 53.3 km at Station SA47 in the Bushveld complex, with a mean value of  $40.3 \pm 4.0$  km. Relatively thin crust is observed in the Cape Fold Belt, central and southern Kaapvaal craton, and northern Zimbabwe craton. The crust thickens within the Namaqua-Natal mobile belt, the Bushveld complex, the Limpopo belt, and the southwestern Zimbabwe craton.

### 3.4. Joint Inversion Results

To more realistically reveal the velocity distribution at a given depth, we jointly inverted Rayleigh wave phase velocity dispersion and RF measurements to obtain shear wave velocities beneath each of the stations.

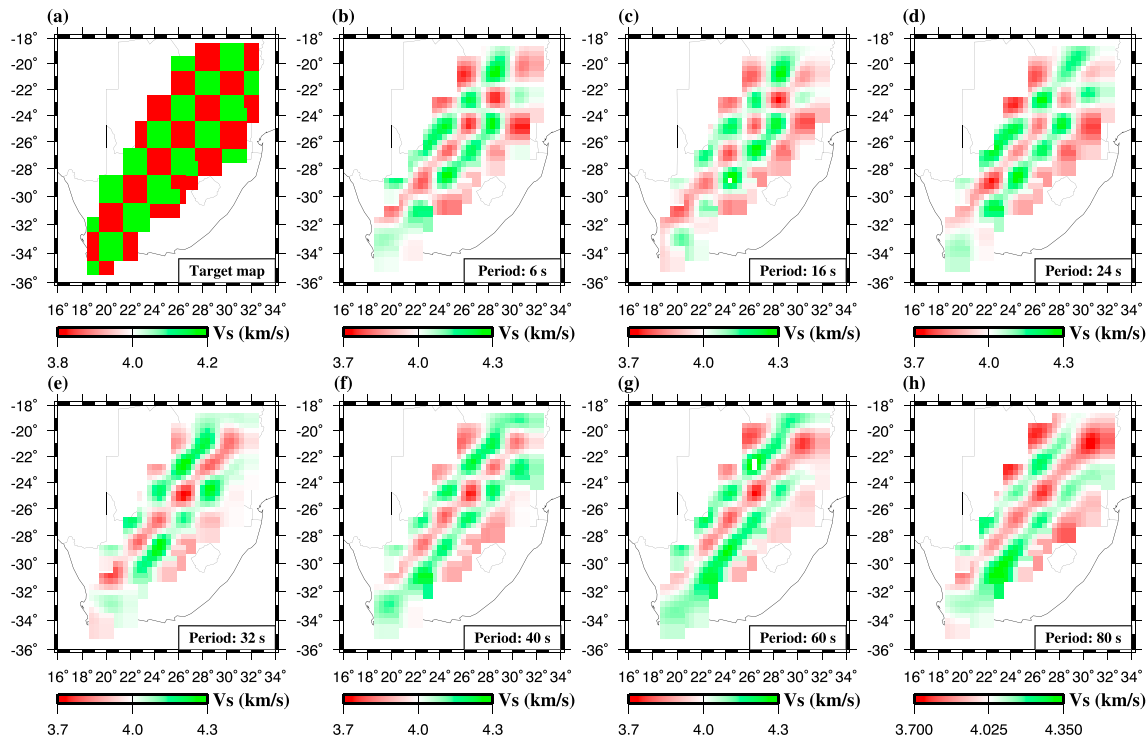


**Figure 7.** Horizontal checkerboard model (a) and its reconstructions (b–h) at different periods. The color bar in (a) represents velocities with both positive and negative 5% perturbations compared with a reference velocity of 4 km/s. (a) Target checkerboard model. (b–d) Recovered velocity results from the empirical Green's function analysis for the periods of 6, 16, and 24 s, respectively. (e–h) Recovered velocity results from the two-station analysis for the periods of 32, 40, 60, and 80 s, respectively.

Figure 9 shows the input data and results for the joint inversion for two of the stations. Note that because the velocity model has only one interface (the Moho), the fitting to the RF is poor except for the time window containing the *PmS* phase. The resulting velocities and crustal thickness measurements observed at individual stations were linearly interpolated to obtain spatially continuous images (Figures 8 and 10–12).

### 3.4.1. Shear Wave Velocity Structures

At the depth of 6 km, low shear wave velocity anomalies are mainly observed beneath the northern and eastern parts of the Kaapvaal craton, the Namaqua-Natal mobile belt, and the Cape Fold Belt in the uppermost

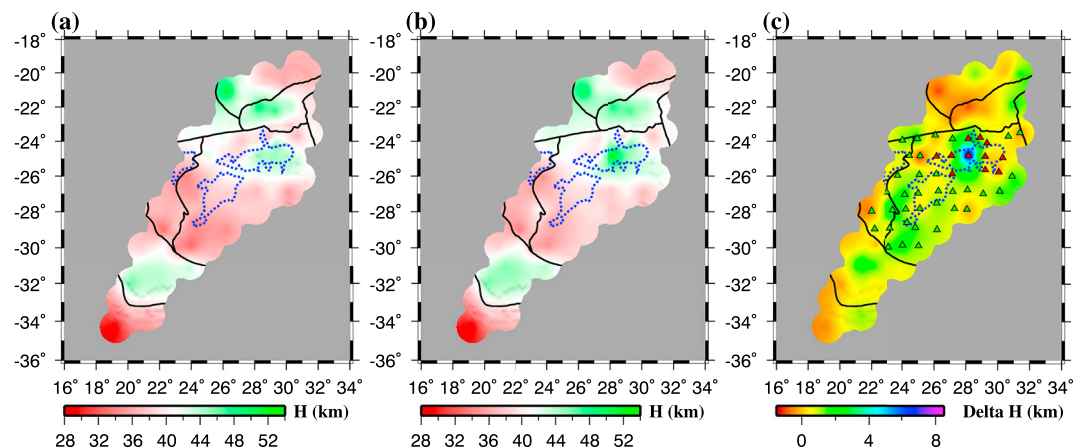


**Figure 8.** Crustal thickness measurements. (a) Results from the joint Bayesian Monte Carlo inversion approach. (b) Results from  $H - \kappa$  stacking of receiver functions. (c) Difference between results shown in (a) and (b). Red triangles represent stations within or close to the Bushveld complex, and green ones represent the rest of the stations within the Kaapvaal craton.

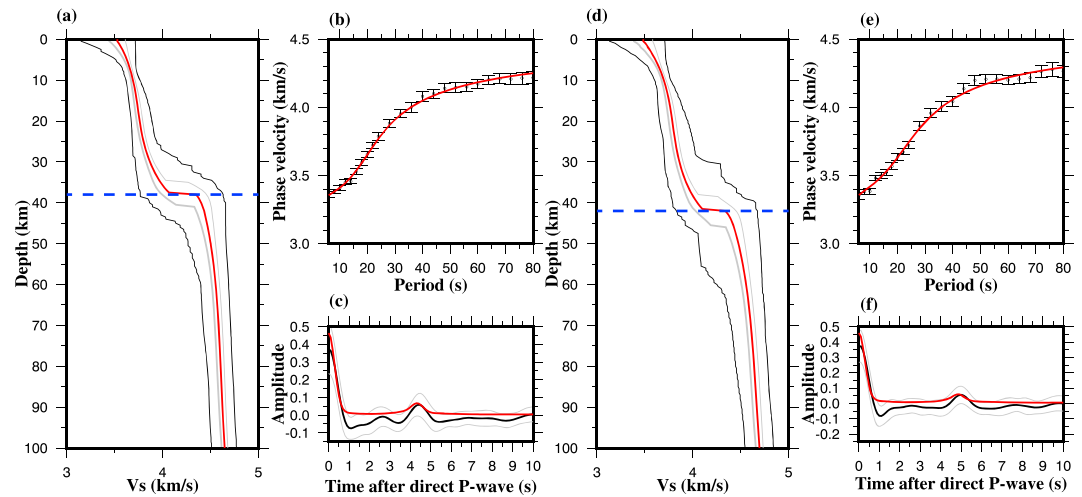


**Figure 9.** Joint inversion results for stations SA38 (a–c) and SA55 (d–f). (a) Ensemble of accepted models using the joint inversion approach for Station SA38. The full width of the ensemble is presented as the black curves, the  $1\sigma$  width of the ensemble under the assumption of Gaussian distribution is presented as light gray curves enclosing the area between the two curves, and the average model is the red curve near the middle of the ensemble. The horizontal blue dash line indicates the crustal thickness beneath the station. (b) Observed Rayleigh wave phase velocities (dots) and  $1\sigma$  error bars for Station SA38. The red curve represents the prediction from the best fitting model in (a). (c) Stacked RF trace (black curve) and the  $1\sigma$  uncertainty (light gray curves) for Station SA38. The red curve is the predicted RF from the best fitting model in (a). (d–f) The same as (a)–(c), but for Station SA55.

crust (Figures 10a and 11a) and are mostly related to the presence of a thick sedimentary cover. At the depth of 20 km (Figure 10b), the Cape Fold Belt continues to demonstrate low velocities, and the Namaqua-Natal mobile belt shows higher velocities relative to the Kaapvaal craton.

Velocity variations in the depths of 30 and 40 km (Figures 10c and 10d) are mainly affected by the depth variation of the Moho discontinuity, where sudden increase in velocity appears in areas with a crust that is shallower than the depth of the slice. At the depth of 30 km (Figure 10c), velocities as fast as  $\sim 4.15$  km/s are observed beneath the southern tip of the Cape Fold Belt, suggesting that the crust in this area is thinner than 30 km. Similarly, beneath the central and southern Kaapvaal craton and northeastern Zimbabwe craton, the high velocities observed in Figure 10d indicate that the crust is thinner than 40 km. Relative to the adjacent mobile belts, the Kaapvaal and Zimbabwe cratons show higher velocities from 50–100 km, while the Cape Fold Belt is characterized by relatively low velocities in the same depth range. A zone of high velocities along the southern margin of the Namaqua-Natal mobile belt persists in the depth range of 50–100 km. The sheet-like shape of the high-velocity feature can be more clearly observed along the cross section shown in Figure 11a.

### 3.4.2. Crustal Thickness Distribution

Based on the assumption that the Moho is a sharp gradient interface across which the shear wave velocity experiences the most rapid increase, we obtained the  $H$  measurements beneath the seismic stations by searching for the largest velocity gradient within the depth range of 20 to 60 km from the inverted 1-D shear wave velocity curve for each of the stations.

The resulting  $H$  values from the joint inversion (Figure 8a) range from 28.5 km at Station SA01 at the southern tip of the Cape Fold Belt to 52.0 km at Station SA70 located at the southwest corner of the Zimbabwe craton, with a mean value of  $39.5 \pm 4.0$  km over the entire study area. For most of the stations, the crustal thickness difference obtained using the joint inversion (Figure 8a) and  $H - \kappa$  stacking (Figure 8b) is less than 3 km (Figure 8c) and are in general agreement with previous crustal thickness studies (Delph & Porter, 2015; Kgaswane et al., 2009; Nair et al., 2006; Yang et al., 2008; Youssof et al., 2013). Both the Kaapvaal and Zimbabwe cratons are characterized by a crustal thickness of about 36 km, which is typical for cratons (e.g., Clitheroe et al., 2000; Nair et al., 2006). Thicker than normal crust is found in the Bushveld complex, the Limpopo belt, and southwestern Zimbabwe craton, and the Namaqua-Natal mobile belt, while the Cape Fold Belt has the thinnest crust of less than 30 km.

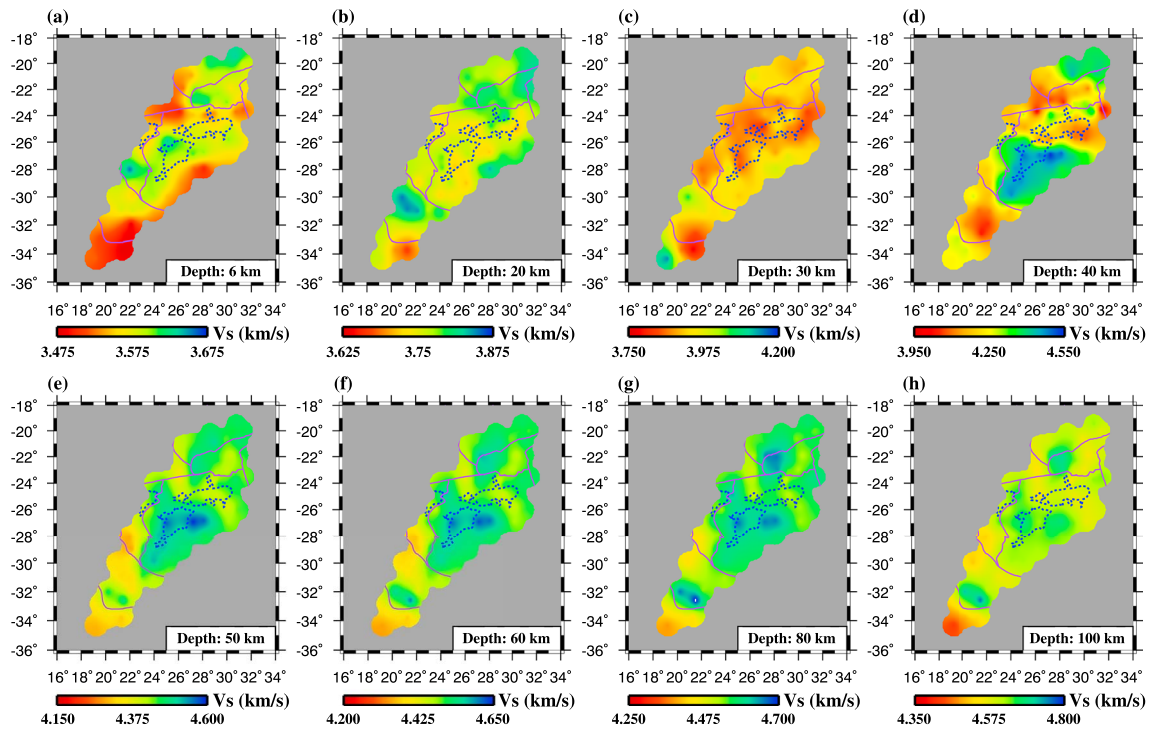


**Figure 10.** Horizontal shear wave velocity slices at different depths: (a) 6, (b) 20, (c) 30, (d) 40, (e) 50, (f) 60, (g) 80, and (h) 100 km.

## 4. Discussion

### 4.1. Basalt Removal in the Kaapvaal Craton

The Kaapvaal craton, with the exception of the Bushveld complex, is characterized by shear wave velocities of about 4.6 km/s, which is about 3% higher than the  $\sim 4.47$  km/s value in most global models such as AK135 (e.g., Kennett et al., 1995). This increase in seismic velocities and the corresponding decrease in the density of the mantle lithosphere (see Figure 12 in Artemieva & Vinnik, 2016) are consistent with the basalt removal model for the formation of continental tectosphere (Jordan, 1979, 1988). However, more recent studies (e.g., Schutt & Leshner, 2006) indicate that the actual velocity increase due to basalt removal is a function of pressure, and at the upper-lithospheric depth, the magnitude of velocity increase due to the removal is less than what was predicted in Jordan (1979). Therefore, other processes, such as the loss of volatiles and grain size changes (Faul & Jackson, 2005; Karato & Jung, 1998) might also play a role in the observed velocity increase beneath the Kaapvaal Craton. Lateral variations of lithospheric temperature probably related to Mesozoic lithospheric delamination/relamination (Hu et al., 2018) may also contribute to the velocity anomalies.

### 4.2. Lithospheric Modification in the Southwestern Zimbabwe Craton by the Okavango Dyke Swarm

The resulting  $H$  measurements for the Zimbabwe craton (Figure 8a) demonstrate a large difference between the northeastern (NE) and southwestern (SW) portions of the craton. The former has a relatively thin crust with a mean value of  $36.8 \pm 1.3$  km, and the latter has a thicker crust of  $44.8 \pm 5.1$  km. In addition, on the depth slides of 50–60 km (Figures 10e and 10f), the mean shear wave velocities beneath the SW Zimbabwe craton is about 0.9% lower than that beneath the NE part of the craton. The SW portion of the craton also shows a higher lithospheric density than the NE part (Artemieva & Vinnik, 2016).

One of the possible causes of the thickened crust, reduced upper mantle velocities, and the increased mantle density beneath the SW Zimbabwe craton is the emplacement of the mafic Okavango dyke swarm at about 179 Ma (Delph & Porter, 2015; Le Gall et al., 2005; Reeves, 2000; Youssof et al., 2013). The observed crustal thickening can be reasonably attributed to massive magmatic intrusion into the crust and magmatic underplating beneath the original Moho associated with the dyke swarm event. The intrusion of the mafic dykes into the subcrustal lithosphere could also result in lithospheric refertilization, leading to the observed

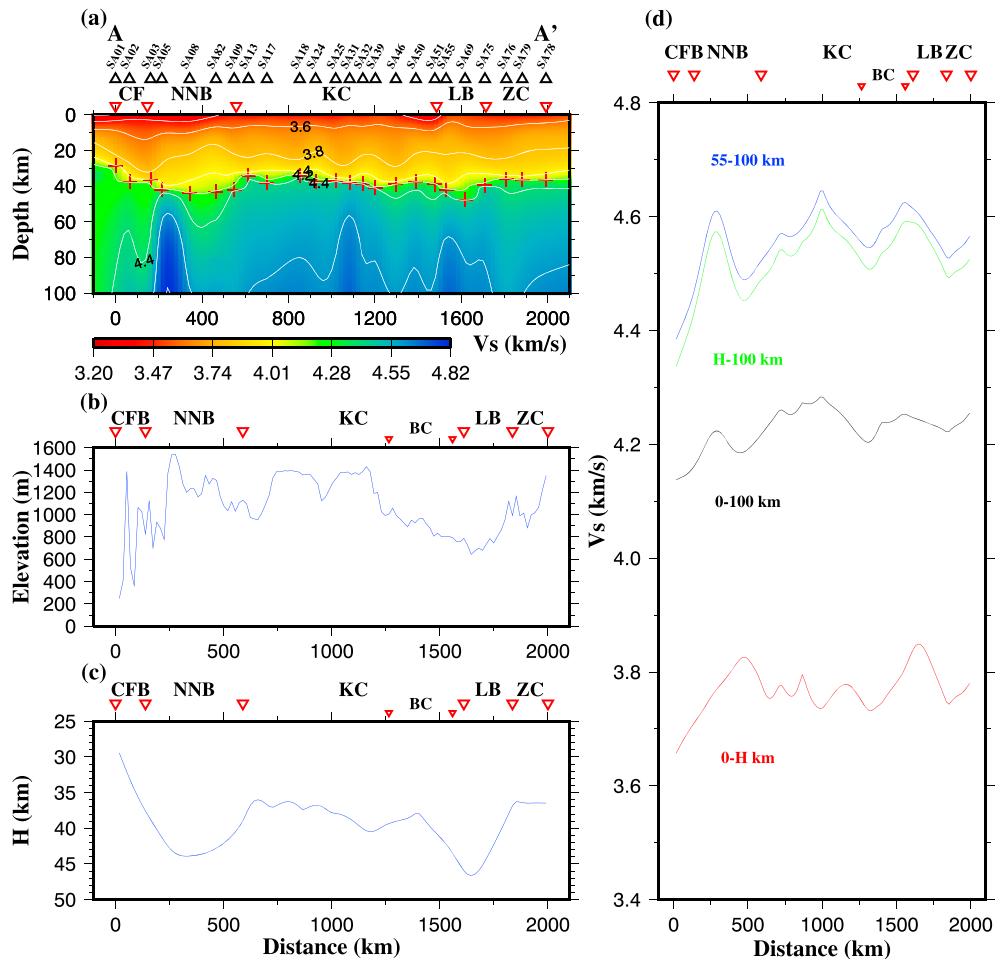


**Figure 11.** (a) Vertical S wave velocity cross section from surface to the depth of 100 km along Profile A-A' in Figure 1. The crosses represent crustal thickness beneath the stations from the joint inversion method. (b) Elevation along the Profile A-A'. (c) Variation of crustal thickness from joint inversion along Profile A-A'. (d) Variation of mean S wave velocities for four depth ranges.

reduction in seismic velocities (Figures 10e and 10f) and increase in mantle density (Artemieva & Vinnik, 2016; Jordan, 1979). The observed amplitude of velocity decrease (about 0.9%) in the uppermost mantle lithosphere beneath the SW Zimbabwe craton is consistent with the estimated velocity decrease due to lithospheric refertilization (Jordan, 1979). Finally, the increase in the density of the subcrustal lithosphere due to the refertilization compensates the mass deficit associated with the thickened crust, resulting in the near zero isostatic gravity anomaly in the area (Gwavava et al., 1996).

#### 4.3. Magmatic Underplating and Lithospheric Refertilization Beneath the Bushveld Complex

Relative to the surrounding cratonic area, the crust beneath the Bushveld complex has a thickness that is about 5 km greater (Figure 8a). Similar to the SW Zimbabwe craton, the shear wave velocity in the subcrustal lithosphere beneath the Bushveld complex is lower than that in the southern Kaapvaal craton (Figure 12), and the lithospheric density is higher (Artemieva & Vinnik, 2016). All the above observations can be explained by intrusion and underplating of mantle-derived materials into the crust as well as refertilization of the lithosphere by the mafic intrusion occurred at 2.05 Ga (de Wit et al., 1992; James et al., 2001; Jordan, 1979; Li & Burke, 2006; Schouwstra et al., 2000). Another possible cause for the lower velocities is higher temperature associated with lithospheric modification in the Mesozoic (Hu et al., 2018).

#### 4.4. Lower Crustal Eclogitization Beneath the Limpopo Belt

Relative to the Kaapvaal craton, the Limpopo belt is characterized by a lower elevation (Figure 11b), thicker crust (Figures 8 and 11c), and higher crustal shear wave velocities (Figures 11d and 12b). In contrast, another

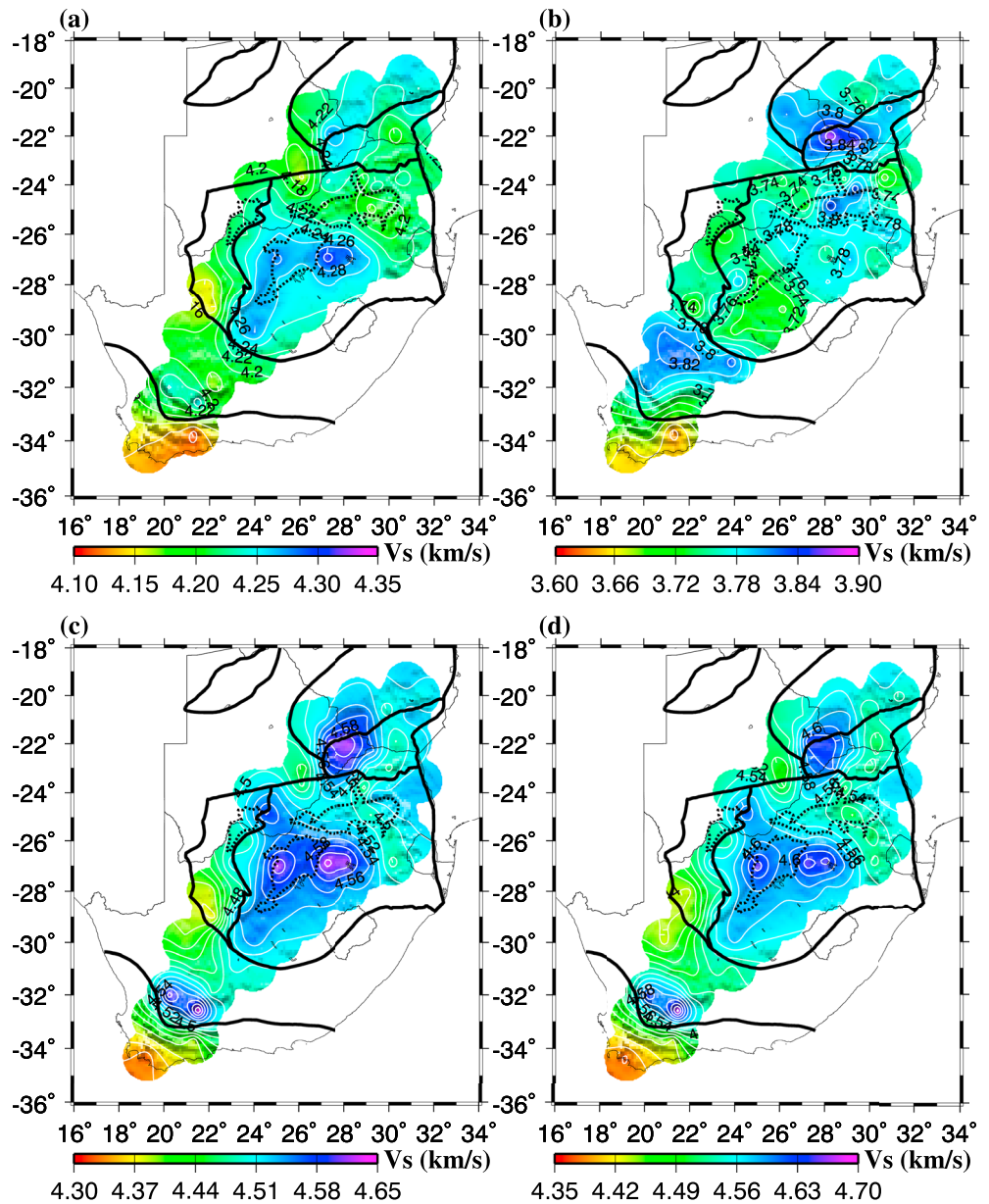


**Figure 12.** Mean shear wave velocities. (a) From the surface to 100-km depth. (b) From the surface to the Moho. (c) From the Moho to 100-km depth. (d) From 55- to 100-km depth.

area with thick crust, the Proterozoic Namaqua-Natal mobile belt (Figures 8 and 11c), has a higher elevation than the Kaapvaal craton (Figure 11b), and a slightly higher crustal shear wave velocity (Figures 11d and 12). The counter-intuitive relationship between the lower elevation and thicker crust beneath the Limpopo belt can be explained by the existence of a high density, probably eclogitized lower crustal layer.

It has been recognized that the less dense gabbro (density = 3.0 g/cm<sup>3</sup>,  $V_p$  = 6.9 km/s) in the lower continental crust can be transformed into more dense eclogite (density = 3.5 g/cm<sup>3</sup>,  $V_p$  = 7.9–8.05 km/s) in tectonically overthickened crust (e.g., Kay & Mahlburg-Kay, 1991; Kern et al., 1999; Ringwood, 1975). Such an eclogitized layer has been revealed in many regions in the world (e.g., Keller, 2013; Rumpfhuber & Keller, 2009). Bouguer gravity anomalies (Ranganai et al., 2002) are relatively higher in the Limpopo belt than the adjacent Zimbabwe and Kaapvaal cratons, providing independent evidence for the presence of a high density crustal layer.

#### 4.5. A Possible Fossil Oceanic Slab Beneath the Southern Namaqua-Natal Mobile Belt

A high-velocity anomaly is consistently present beneath the southern Namaqua-Natal Mobile Belt in the 50- to 100-km depth range (Figures 10e–10h). From the cross section (Figure 11a) and velocities at various depth ranges (Figure 12), it is clear that this feature extends from beneath the Moho to at least 100-km depth. We speculate that this high-velocity feature is a fossil oceanic slab beneath the suture zone with the Cape Fold Belt to the south. The assimilation of the Cape Fold Belt occurred during 800–1000 Ma and prior to the assimilation, there existed an oceanic plate (de Beer et al., 1982; Lock, 1980). Such high-velocity belts in the lithosphere have been identified on the edges of other cratonic blocks (e.g., Bostock, 1997, for the Slave Craton) and might reflect the velocity difference associated with the variation in chemical composition between the oceanic and continental lithosphere. This hypothesis is consistent with the observation that the oceanic lithosphere is more mafic than the continental lithosphere and possesses higher shear wave velocities (Boyd, 1989).

### 5. Conclusions

Three-dimensional distributions of shear wave velocities in the top 100 km of the lithosphere beneath two of the oldest cratons on Earth and orogenic belts of various ages are revealed using ambient noise and earthquake surface wave tomography, with constraints from *P*-to-*S* RFs. The observations provide constraints on a number of significant problems regarding continental lithospheric structure and evolution. The unmodified area of the Kaapvaal craton is characterized by high mantle velocities which are consistent with the basalt removal for the formation of continental tectosphere. Crustal thickening and higher crustal velocities beneath the SW Zimbabwe craton and the Bushveld complex can be explained by magmatic intrusion and underplating, and the observed lower velocity and higher density in the mantle lithosphere beneath the two magmatically modified areas are most likely the results of mantle refertilization. While a thicker crustal root is found to correspond with the higher elevation beneath the Proterozoic Namaqua-Natal mobile belt, the thicker crust found beneath the lower elevation Archean Limpopo belt is probably at least partially compensated by a high density lower crustal layer which could be resulted from eclogitization of the gabbro-rich lower crust. We interpret a high-velocity zone along the southern margin of the Namaqua-Natal mobile belt as a segment of stalled oceanic lithosphere.

#### Acknowledgments

All the seismic waveform data used in the study were obtained from the IRIS DMC and are publicly accessible (<https://ds.iris.edu/ds/nodes/dmc>; last accessed: May 2018). We thank Z. Eilon, an anonymous reviewer, and Editor Maureen Long for their careful reviews of the manuscript. The study was partially supported by the U.S. National Science Foundation under Grants 1009946 and 1321656 to K.L. and S.G.

#### References

- Adams, A., & Nyblade, A. (2011). Shear wave velocity structure of the southern African upper mantle with implications for the uplift of southern Africa. *Geophysical Journal International*, *186*(2), 808–824. <https://doi.org/10.1111/j.1365-246X.2011.05072.x>
- Ammon, C. J., Randall, G. E., & Zandt, G. (1990). On the nonuniqueness of receiver function inversions. *Journal of Geophysical Research*, *95*(B10), 15,303–15,318. <https://doi.org/10.1029/JB095iB10p15303>
- Artemieva, I. M., & Vinnik, L. P. (2016). Density structure of the cratonic mantle in Southern Africa: 2. Correlations with kimberlite distribution, seismic velocities, and Moho sharpness. *Gondwana Research*, *36*, 14–27. <https://doi.org/10.1016/j.gr.2016.05.002>
- Bensen, G. D., Ritzwoller, M. H., Barmin, M. P., Levshin, A. L., Lin, F., Moschetti, M. P., et al. (2007). Processing seismic ambient noise data to obtain reliable broad-band surface wave dispersion measurements. *Geophysical Journal International*, *169*(3), 1239–1260. <https://doi.org/10.1111/j.1365-246X.2007.03374.x>
- Bodin, T., Sambridge, M., Tkalcic, H., Arroucau, P., Gallagher, K., & Rawlinson, N. (2012). Transdimensional inversion of receiver functions and surface wave dispersion. *Journal of Geophysical Research*, *117*, B02301. <https://doi.org/10.1029/2011JB008560>
- Bostock, M. G. (1997). Anisotropic upper-mantle stratigraphy and architecture of the Slave craton. *Nature*, *390*, 392–395. <https://doi.org/10.1038/37102>
- Boyd, F. R. (1989). Compositional distinction between oceanic and cratonic lithosphere. *Earth and Planetary Science Letters*, *96*(1–2), 15–26. [https://doi.org/10.1016/0012-821X\(89\)90120-9](https://doi.org/10.1016/0012-821X(89)90120-9)
- Buick, I. S., Maas, R., & Gibson, R. (2001). Precise U-Pb titanite age constraints on the emplacement of the Bushveld Complex, South Africa. *Journal of the Geological Society*, *158*(1), 3–6. <https://doi.org/10.1144/jgs.158.1.3>
- Christensen, N. I., & Mooney, W. D. (1995). Seismic velocity structure and composition of the continental crust: A global view. *Journal of Geophysical Research*, *100*(B6), 9761–9788. <https://doi.org/10.1029/95JB00259>
- Clitheroe, G., Gudmundsson, O., & Kennett, B. L. N. (2000). The crustal thickness of Australia. *Journal of Geophysical Research*, *105*(B6), 13,697–13,713. <https://doi.org/10.1029/1999JB900317>
- Compston, W., & Kroner, A. (1988). Multiple zircon growth within early Archean tonalitic gneiss from the Ancient Gneiss Complex, Swaziland. *Earth and Planetary Science Letters*, *87*(1–2), 13–28. [https://doi.org/10.1016/0012-821X\(88\)90061-1](https://doi.org/10.1016/0012-821X(88)90061-1)
- de Beer, J. H., van Zijl, J. S. V., & Gough, D. I. (1982). The southern cape conductive belt (South Africa): Its composition, origin and tectonic significance. *Tectonophysics*, *83*(3–4), 205–225. [https://doi.org/10.1016/0040-1951\(82\)90019-1](https://doi.org/10.1016/0040-1951(82)90019-1)
- de Wit, M. J., de Ronde, C. E. J., Tredoux, M., Roering, C., Hart, R. J., Armstrong, R. A., et al. (1992). Formation of an Archean continent. *Nature*, *357*, 553–562. <https://doi.org/10.1038/357553a0>
- de Wit, M., & Tinker, J. (2004). Crustal structures across the central Kaapvaal craton from deep-seismic reflection data. *South African Journal of Geology*, *107*(1–2), 185–206. <https://doi.org/10.2113/107.1-2.185>
- Delph, J. R., & Porter, R. C. (2015). Crustal structure beneath southern Africa: Insight into how tectonic events affect the Mohorovicic discontinuity. *Geophysical Journal International*, *200*(1), 254–264. <https://doi.org/10.1093/gji/ggu376>

- Deng, Y., Shen, W., Xu, T., & Ritzwoller, M. H. (2015). Crustal layering in northeastern Tibet: A case study based on joint inversion of receiver functions and surface wave dispersion. *Geophysical Journal International*, 203(1), 692–706. <https://doi.org/10.1093/gji/ggv321>
- Durrheim, R. J., & Green, R. W. E. (1992). A seismic refraction investigation of the Archaean Kapaavaal Craton, South Africa, using mine tremors as the energy source. *Geophysical Journal International*, 108(3), 812–832. <https://doi.org/10.1111/j.1365-246X.1992.tb03472.x>
- Durrheim, R. J., & Mooney, W. D. (1994). Evolution of the Precambrian lithosphere: Seismological and geochemical constraints. *Journal of Geophysical Research*, 99(B8), 15,359–15,374. <https://doi.org/10.1029/94JB00138>
- Dziewonski, A. M., & Anderson, D. L. (1981). Preliminary reference Earth model. *Physics of the Earth and Planetary Interiors*, 25(4), 297–356. [https://doi.org/10.1016/0031-9201\(81\)90046-7](https://doi.org/10.1016/0031-9201(81)90046-7)
- Dziewonski, A., Bloch, S., & Landisman, M. (1969). A technique for the analysis of transient seismic signals. *Bulletin of the Seismological Society of America*, 59(1), 427–444.
- Efron, B., & Tibshirani, R. (1986). Bootstrap methods for standard errors, confidence intervals, and other measures of statistical accuracy. *Statistical Science*, 1(1), 54–75. <https://doi.org/10.1214/ss/1177013815>
- Faul, U. H., & Jackson, I. (2005). The seismological signature of temperature and grain size variations in the upper mantle. *Earth and Planetary Science Letters*, 234(1–2), 119–134. <https://doi.org/10.1016/j.epsl.2005.02.008>
- Gao, S. S., & Liu, K. H. (2014). Mantle transition zone discontinuities beneath the contiguous United States. *Journal of Geophysical Research: Solid Earth*, 119, 6452–6468. <https://doi.org/10.1002/2014JB011253>
- Green, R. W. E., & Durrheim, R. J. (1990). A seismic refraction investigation of the Namaqualand Metamorphic Complex, South Africa. *Journal of Geophysical Research*, 95(B12), 19,927–19,932. <https://doi.org/10.1029/JB095iB12p19927>
- Gwavava, O., Swain, C. J., & Podmore, F. (1996). Mechanisms of isostatic compensation of the Zimbabwe and Kapaavaal cratons, the Limpopo Belt and the Mozambique basin. *Geophysical Journal International*, 127(3), 635–650. <https://doi.org/10.1111/j.1365-246X.1996.tb04044.x>
- Hamilton, P. J., Evensen, N. M., O’Nions, R. K., Smith, H. S., & Erlank, A. J. (1979). Sm-Nd dating of Onverwacht Group volcanics, southern Africa. *Nature*, 279, 298–300. <https://doi.org/10.1038/279298a0>
- Hickman, M. H. (1978). Isotopic evidence for crystal reworking in the Rhodesian Archean craton, southern Africa. *Geology*, 6(4), 214–216. [https://doi.org/10.1130/0091-7613\(1978\)6<214:IEFCRI>2.0.CO;2](https://doi.org/10.1130/0091-7613(1978)6<214:IEFCRI>2.0.CO;2)
- Hu, J., Liu, L., Faccenda, M., Zhou, Q., Fischer, K. M., Marshak, S., & Lundstrom, C. (2018). Modification of the Western Gondwana craton by plume-lithosphere interaction. *Nature Geoscience*, 11, 203–210.
- James, D. E., Fouch, M. J., VanDecar, J. C., van der Lee, S., & Kapaavaal Seismic Group (2001). Tectospheric structure beneath southern Africa. *Geophysical Research Letters*, 28(13), 2485–2488. <https://doi.org/10.1029/2000GL012578>
- Jelsma, H. A., & Dirks, P. H. G. M. (2002). Neoarchaean tectonic evolution of the Zimbabwe Craton. *Geological Society, London, Special Publications*, 199, 183–211. <https://doi.org/10.1144/GSL.SP.2002.199.01.10>
- Jordan, T. H. (1979). Mineralogies, densities, and seismic velocities of garnet lherzolites and their geophysical implications, *In The Mantle Sample: Inclusion in Kimberlites and Other Volcanics* (Vol. 16, pp. 1–14). Washington, DC: American Geophysical Union. <https://doi.org/10.1029/SP016p0001>
- Jordan, T. H. (1988). Structure and formation of the continental tectosphere. *Journal of Petrology, Special\_Volume*(1), 11–37. [https://doi.org/10.1093/ptrology/Special\\_Volume.1.11](https://doi.org/10.1093/ptrology/Special_Volume.1.11)
- Julia, J., Ammon, C. J., Herrmann, R. B., & Correig, A. M. (2000). Joint inversion of receiver function and surface wave dispersion observations. *Geophysical Journal International*, 143(1), 99–112. <https://doi.org/10.1046/j.1365-246X.2000.00217.x>
- Julia, J., Ammon, C. J., & Nyblade, A. A. (2005). Evidence for mafic lower crust in Tanzania, East Africa, from joint inversion of receiver functions and Rayleigh wave dispersion velocities. *Geophysical Journal International*, 162(2), 555–569. <https://doi.org/10.1111/j.1365-246X.2005.02685.x>
- Kanamori, H., & Anderson, D. L. (1977). Importance of physical dispersion in surface wave and free oscillation problems: Review. *Reviews of Geophysics*, 15(1), 105–112. <https://doi.org/10.1029/RG015i001p00105>
- Karato, S.-I. (1993). Importance of anelasticity in the interpretation of seismic tomography. *Geophysical Research Letters*, 20(15), 1623–1626. <https://doi.org/10.1029/93GL01767>
- Karato, S.-i., & Jung, H. (1998). Water, partial melting and the origin of the seismic low velocity and high attenuation zone in the upper mantle. *Earth and Planetary Science Letters*, 157(3–4), 193–207. [https://doi.org/10.1016/S0012-821X\(98\)00034-X](https://doi.org/10.1016/S0012-821X(98)00034-X)
- Kay, R. W., & Mahlburg-Kay, S. (1991). Creation and destruction of lower continental crust. *Geologische Rundschau*, 80(2), 259–278.
- Keller, G. R. (2013). The Moho of North America: A brief review focused on recent studies. *Tectonophysics*, 609, 45–55. <https://doi.org/10.1016/j.tecto.2013.07.031>
- Kennett, B. L. N., & Engdahl, E. R. (1991). Traveltimes for global earthquake location and phase identification. *Geophysical Journal International*, 105(2), 429–465. <https://doi.org/10.1111/j.1365-246X.1991.tb06724.x>
- Kennett, B. L. N., Engdahl, E. R., & Buland, R. (1995). Constraints on seismic velocities in the Earth from traveltimes. *Geophysical Journal International*, 122(1), 108–124. <https://doi.org/10.1111/j.1365-246X.1995.tb03540.x>
- Kern, H., Gao, S., Jin, Z., Popp, T., & Jin, S. (1999). Petrophysical studies on rocks from the Dabie ultrahigh-pressure (UHP) metamorphic belt, Central China: Implications for the composition and delamination of the lower crust. *Tectonophysics*, 301(3–4), 191–215. [https://doi.org/10.1016/S0040-1951\(98\)00268-6](https://doi.org/10.1016/S0040-1951(98)00268-6)
- Kgaswane, E. M., Nyblade, A. A., Julia, J., Dirks, P. H. G. M., Durrheim, R. J., & Pasyanos, M. E. (2009). Shear wave velocity structure of the lower crust in southern Africa: Evidence for compositional heterogeneity within Archaean and Proterozoic terrains. *Journal of Geophysical Research*, 114, B12304. <https://doi.org/10.1029/2008JB006217>
- Kroner, A., Hegner, E., Wendt, J. I., & Byerly, G. R. (1996). The oldest part of the Barberton granitoid-greenstone terrain, South Africa: evidence for crust formation between 3.5 and 3.7 Ga. *Precambrian Research*, 78(1–3), 105–124. [https://doi.org/10.1016/0301-9268\(95\)00072-0](https://doi.org/10.1016/0301-9268(95)00072-0)
- Le Gall, B., Tshoso, G., Dymont, J., Kampunzu, A. B., Jourdan, F., Feraud, G., et al. (2005). The Okavango giant mafic dyke swarm (NE Botswana): Its structural significance within the Karoo Large Igneous Province. *Journal of Structural Geology*, 27(12), 2234–2255. <https://doi.org/10.1016/j.jsg.2005.07.004>
- Le Gall, B., Tshoso, G., Jourdan, F., Feraud, G., Bertrand, H., Tiercelin, J. J., et al. (2002). <sup>40</sup>Ar/<sup>39</sup>Ar geochronology and structural data from the giant Okavango and related mafic dyke swarms, Karoo igneous province, northern Botswana. *Earth and Planetary Science Letters*, 202(3–4), 595–606. [https://doi.org/10.1016/S0012-821X\(02\)00763-X](https://doi.org/10.1016/S0012-821X(02)00763-X)
- Li, A. (2011). Shear wave model of southern Africa from regional Rayleigh wave tomography with 2-D sensitivity kernels. *Geophysical Journal International*, 185(2), 832–844. <https://doi.org/10.1111/j.1365-246X.2011.04971.x>
- Li, A., & Burke, K. (2006). Upper mantle structure of southern Africa from Rayleigh wave tomography. *Journal of Geophysical Research*, 111, B10303. <https://doi.org/10.1029/2006JB004321>



- Liu, K. H., & Gao, S. S. (2010). Spatial variations of crustal characteristics beneath the Hoggar swell, Algeria, revealed by systematic analyses of receiver functions from a single seismic station. *Geochemistry, Geophysics, Geosystems*, *11*, Q08011. <https://doi.org/10.1029/2010GC003091>
- Lock, B. E. (1980). Flat-plate subduction and the Cape Fold Belt of South Africa. *Geology*, *8*(1), 35–39. [https://doi.org/10.1130/0091-7613\(1980\)8<35:FSATCF>2.0.CO;2](https://doi.org/10.1130/0091-7613(1980)8<35:FSATCF>2.0.CO;2)
- Nair, S. K., Gao, S. S., Liu, K. H., & Silver, P. G. (2006). Southern African crustal evolution and composition: Constraints from receiver function studies. *Journal of Geophysical Research*, *111*, B02304. <https://doi.org/10.1029/2005JB003802>
- Ozalaybey, S., Savage, M. K., Sheehan, A. F., Louie, J. N., & Brune, J. N. (1997). Shear-wave velocity structure in the northern basin and Range province from combined analysis of receiver functions and surface waves. *Bulletin of the Seismological Society of America*, *87*(1), 183–199.
- Press, W. H., Teukolsky, S. A., Vetterling, W. T., & Flannery, B. P. (1992). *Numerical recipes in FORTRAN* (2nd ed.). New York: Cambridge University Press.
- Ranganai, R. T., Kampunzu, A. B., Atekwana, E. A., Paya, B. K., King, J. G., Koosimile, D. I., & Stettler, E. H. (2002). Gravity evidence for a larger Limpopo Belt in southern Africa and geodynamic implications. *Geophysical Journal International*, *149*(3), F9–F14. <https://doi.org/10.1046/j.1365-246X.2002.01703.x>
- Ravenna, M., Lebedev, S., Fullea, J., & Adam, J. M.-C. (2018). Shear-wave velocity structure of southern Africa's lithosphere: Variations in the thickness and composition of cratons and their effect on topography. *Geochemistry, Geophysics, Geosystems*, *19*, 1499–1518. <https://doi.org/10.1029/2017GC007399>
- Reeves, C. (2000). The geophysical mapping of Mesozoic dyke swarms in southern Africa and their origin in the disruption of Gondwana. *Journal of African Earth Sciences*, *30*(3), 499–513. [https://doi.org/10.1016/S0899-5362\(00\)00035-X](https://doi.org/10.1016/S0899-5362(00)00035-X)
- Ringwood, A. E. (1975). *Composition and Petrology of the Earth's Mantle* (1st ed., pp. 672). New York: McGraw-Hill.
- Rozendaal, A., Gresse, P. G., Scheepers, R., & Le Roux, J. P. (1999). Neoproterozoic to Early Cambrian crustal evolution of the Pan-African Saldania Belt, South Africa. *Precambrian Research*, *97*(3-4), 303–323. [https://doi.org/10.1016/S0301-9268\(99\)00036-4](https://doi.org/10.1016/S0301-9268(99)00036-4)
- Rumpfhuber, E.-M., & Keller, G. R. (2009). An integrated analysis of controlled and passive source seismic data across an Archean-Proterozoic suture zone in the Rocky Mountains. *Journal of Geophysical Research*, *114*, B08305. <https://doi.org/10.1029/2008JB005886>
- Sabra, K. G., Gerstoft, P., Roux, P., Kuperman, W. A., & Fehler, M. C. (2005). Extracting time-domain Green's function estimates from ambient seismic noise. *Geophysical Research Letters*, *32*, L03310. <https://doi.org/10.1029/2004GL021862>
- Schouwstra, R. P., Kinloch, E. D., & Lee, C. A. (2000). A short geological review of the Bushveld complex. *Platinum Metals Review*, *44*(1), 33–39.
- Schutt, D. L., & Leshner, C. E. (2006). Effects of melt depletion on the density and seismic velocity of garnet and spinel lherzolite. *Journal of Geophysical Research*, *111*, B05401. <https://doi.org/10.1029/2003JB002950>
- Shapiro, N. M., & Campillo, M. (2004). Emergence of broadband Rayleigh waves from correlations of the ambient seismic noise. *Geophysical Research Letters*, *31*, L07614. <https://doi.org/10.1029/2004GL019491>
- Shapiro, N. M., Campillo, M., Stehly, L., & Ritzwoller, M. H. (2005). High-resolution surface-wave tomography from ambient seismic noise. *Science*, *307*(5715), 1615–1618. <https://doi.org/10.1126/science.1108339>
- Shapiro, N. M., & Ritzwoller, M. H. (2002). Monte-Carlo inversion for a global shear-velocity model of the crust and upper mantle. *Geophysical Journal International*, *151*(1), 88–105. <https://doi.org/10.1046/j.1365-246X.2002.01742.x>
- Shen, W., & Ritzwoller, M. H. (2016). Crustal and uppermost mantle structure beneath the United States. *Journal of Geophysical Research: Solid Earth*, *121*, 4306–4342. <https://doi.org/10.1002/2016JB012887>
- Shen, W., Ritzwoller, M. H., Schulte-Pelkum, V., & Lin, F.-C. (2013). Joint inversion of surface wave dispersion and receiver functions: A Bayesian Monte-Carlo approach. *Geophysical Journal International*, *192*(2), 807–836. <https://doi.org/10.1093/gji/ggs050>
- Shibutani, T., Sambridge, M., & Kennett, B. (1996). Genetic algorithm inversion for receiver functions with application to crust and uppermost mantle structure beneath eastern Australia. *Geophysical Research Letters*, *23*(14), 1829–1832. <https://doi.org/10.1029/96GL01671>
- Tarantola, A., & Nercessian, A. (1984). Three-dimensional inversion without blocks. *Geophysical Journal International*, *76*(2), 299–306. <https://doi.org/10.1111/j.1365-246X.1984.tb05047.x>
- Tarantola, A., & Valette, B. (1982). Generalized nonlinear inverse problems solved using the least squares criterion. *Reviews of Geophysics*, *20*(2), 219–232. <https://doi.org/10.1029/RG020i002p00219>
- Thomas, R. J., von Veh, M. W., & McCourt, S. (1993). The tectonic evolution of southern Africa: An overview. *Journal of African Earth Sciences*, *16*(1-2), 5–24. [https://doi.org/10.1016/0899-5362\(93\)90159-N](https://doi.org/10.1016/0899-5362(93)90159-N)
- Treloar, P. J., & Blenkinsop, T. G. (1995). Archean deformation patterns in Zimbabwe: true indicators of Tibetan-style crustal extrusion or not? *Geological Society, London, Special Publications*, *95*(1), 87–107. <https://doi.org/10.1144/GSL.SP.1995.095.01.06>
- Uken, R., & Watkeys, M. K. (1997). An interpretation of mafic dyke swarms and their relationship with major mafic magmatic events on the Kaapvaal Craton and Limpopo Belt. *South African Journal of Geology*, *100*(4), 341–348.
- Von Gruenewaldt, G., Sharpe, M. R., & Hatton, C. J. (1985). The Bushveld Complex: Introduction and review. *Economic Geology*, *80*(4), 803–812. <https://doi.org/10.2113/gsecongeo.80.4.803>
- Walraven, F., & Hattingh, E. (1993). Geochronology of the Nebo Granite, Bushveld Complex. *South African Journal of Geology*, *96*(1-2), 31–41.
- Wang, T., Feng, J., Liu, K. H., & Gao, S. S. (2019). Crustal structure beneath the Malawi and Luangwa Rift Zones and adjacent areas from ambient noise tomography. *Gondwana Research*, *67*, 187–198. <https://doi.org/10.1016/j.gr.2018.10.018>
- Weaver, R. L. (2005). Information from seismic noise. *Science*, *307*(5715), 1568–1569. <https://doi.org/10.1126/science.1109834>
- Weaver, R. L., & Lobkis, O. I. (2004). Diffuse fields in open systems and the emergence of the Green's function. *The Journal of the Acoustical Society of America*, *116*(5), 2731–2734. <https://doi.org/10.1121/1.1810232>
- Wilson, J. F. (1990). A craton and its cracks: Some of the behaviour of the Zimbabwe block from the Late Archean to the Mesozoic in response to horizontal movements, and the significance of some of its mafic dyke fracture patterns. *Journal of African Earth Sciences*, *10*(3), 483–501. [https://doi.org/10.1016/0899-5362\(90\)90101-J](https://doi.org/10.1016/0899-5362(90)90101-J)
- Yang, Y., Li, A., & Ritzwoller, M. H. (2008). Crustal and uppermost mantle structure in southern Africa revealed from ambient noise and teleseismic tomography. *Geophysical Journal International*, *174*(1), 235–248. <https://doi.org/10.1111/j.1365-246X.2008.03779.x>
- Yao, H., Beghein, C., & van der Hilst, R. D. (2008). Surface wave array tomography in SE Tibet from ambient seismic noise and two-station analysis—II. Crustal and upper-mantle structure. *Geophysical Journal International*, *173*(1), 205–219. <https://doi.org/10.1111/j.1365-246X.2007.03696.x>

- Yao, H., van der Hilst, R. D., & de Hoop, M. V. (2006). Surface-wave array tomography in SE Tibet from ambient seismic noise and two-station analysis—I. Phase velocity maps. *Geophysical Journal International*, *166*(2), 732–744. <https://doi.org/10.1111/j.1365-246X.2006.03028.x>
- Yao, H., van der Hilst, R. D., & Montagner, J.-P. (2010). Heterogeneity and anisotropy of the lithosphere of SE Tibet from surface wave array tomography. *Journal of Geophysical Research*, *115*, B12307. <https://doi.org/10.1029/2009JB007142>
- Yao, H. J., Xu, G. M., Xiao, X., & Zhu, L. B. (2004). A quick tracing method based on image analysis technique for the determination of dual stations phase velocities dispersion curve of surface wave (in Chinese). *Seismological & Geomagnetic Observation & Research*, *25*(1), 1–8.
- Yao, H., Xu, G., Zhu, L., & Xiao, X. (2005). Mantle structure from inter-station Rayleigh wave dispersion and its tectonic implication in western China and neighboring regions. *Physics of the Earth and Planetary Interiors*, *148*(1), 39–54. <https://doi.org/10.1016/j.pepi.2004.08.006>
- Youssef, M., Thybo, H., Artemieva, I. M., & Levander, A. (2013). Moho depth and crustal composition in Southern Africa. *Tectonophysics*, *609*, 267–287. <https://doi.org/10.1016/j.tecto.2013.09.001>
- Zhu, L., & Kanamori, H. (2000). Moho depth variation in southern California from teleseismic receiver functions. *Journal of Geophysical Research*, *105*(B2), 2969–2980. <https://doi.org/10.1029/1999JB900322>